The Double-Degenerate Nucleus of the Planetary Nebula TS 01. A Close Binary Evolution Showcase.

Gagik Tovmassian[1], Lev Yungelson[2], Thomas Rauch [3], Valery Suleimanov[3*], Ralf Napiwotzki[4], Grazyna Stasińska[5], John Tomsick[6], Jörn Wilms[7], Christophe Morisset[8], Miriam Peña[8], Michael G. Richer[1]

ABSTRACT

We present a detailed investigation of SBS 1150+599A, a close binary star hosted by the planetary nebula PN G135.9+55.9 (TS 01, Stasińska et al. 2009). The nebula, located in the Galactic halo, is the most oxygen-poor one known to date and is the only one known to harbor a double degenerate core. We present XMM-*Newton* observations of this object, which allowed the detection of the previously invisible component of the binary core, whose existence was inferred so far only from radial velocity and photometric variations. The parameters of the binary system were deduced from a wealth of information via three independent routes using the spectral energy distribution (from the infrared to X-rays), the light and radial velocity curves, and a detailed model atmosphere fitting of the stellar absorption features of the optical/UV component. We find that the *cool* component must have a mass of $0.54 \pm 0.2\,M_\odot$, an average effective temperature, $T_{\rm eff}$, of $58\,000 \pm 3\,000$ K, a mean radius of $0.43 \pm 0.3\,R_\odot$, a gravity $\log g = 5.0 \pm 0.3$, and that it nearly fills its Roche lobe. Its surface elemental abundances are found to be: 12 + log He/H = 10.95 ±0.04 dex, 12 + log C/H = 7.20±0.3 dex, 12 + log N/H < 6.92 and 12 + log O/H < 6.80, in overall agreement with the chemical composition of the planetary nebula. The *hot* component has $T_{\rm eff}$ = 160–180 kK, a luminosity of about $\sim 10^4 L_\odot$ and a radius slightly larger than that of a white dwarf. It is probably bloated and heated as a result of intense accretion and nuclear burning on its surface in the past. The total mass of the binary system is very close to Chandrasekhar limit. This makes TS 01 one of the best type Ia supernova progenitor candidates. We propose two possible scenarios for the evolution of the system up to its present stage.

Subject headings: stars: binaries: close: individual(SBS1150+599A): atmospheres: AGB and post-AGB: symbiotic: evolution: supernovae; (ISM:) planetary nebulae: individual (PN G135.9+55.9, TS 01)

1. Introduction

SBS 1150+599A was identified as a planetary nebula (PN) in Tovmassian et al. (2001) and subsequently designated as PN G135.9+55.9. More recently, we refer to this object as TS 01 (Stasińska et al. 2009). The object has unusually few spectral lines for a PN and is renown for its extremely low oxygen content (Tovmassian et al. 2001; Jacoby

[1]Instituto de Astronomia, Universidad Nacional Autonoma de Mexico, Apdo. Postal 877, Ensenada, Baja California, 22800 Mexico.

[2]Institute of Astronomy of the Russian Academy of Sciences, 48 Pyatnitskaya Str., 119017 Moscow, Russia.

[3]Institute for Astronomy and Astrophysics, Kepler Center for Astro and Particle Physics, Eberhard Karls University, Sand 1, 72076 Tübingen, Germany.

[4]Centre for Astrophysics Research, University of Hertfordshire, College Lane, Hateld AL109AB, UK.

[5]LUTH, Observatoire de Paris, CNRS, Université Paris Diderot; Place Jules Janssen 92190 Meudon, France.

[6]Space Sciences Laboratory, 7 Gauss Way, University of California, Berkeley, CA 94720-7450, USA.

[7]Dr. Karl Remeis-Observatory, University of Erlangen-Nuremberg, Sternwartstrasse 7, 96049 Bamberg, Germany.

[8]Instituto de Astronomia, Universidad Nacional Autonoma de Mexico, Apdo. Postal 70264, Mexico D.F., 04510 Mexico.

[*]Kazan State University, Russia.

et al. 2002; Péquignot & Tsamis 2005; Stasińska et al. 2005, 2009). It is located above the Galactic plane at a distance of at least a dozen kpc, which places it among a handful of known halo PNe. Direct images obtained on the ground (Richer et al. 2002; Jacoby et al. 2002), and most recently by HST (Napiwotzki et al. 2005; Stasińska et al. 2009) confirm its PN identification. The observed expansion velocity of the nebula (Richer et al. 2003) is typical of PNe. But another outstanding feature of this PN is that it harbors a close binary system (Tovmassian et al. 2004), revealed serendipitously by the displacement of stellar lines with respect to nebular lines within a single observing night. Since only one component of the binary could be observed in the optical and UV, it was suggested that the visible component has a temperature of 110 000–120 000 K. The lower limit is the minimum effective temperature needed to produce the observed [Ne V] nebular emission line, while the upper limit was deduced from the slope of the continuum (Tovmassian et al. 2004). There was an ambiguity in the determination of the orbital period, although it was clear that the nucleus is a close binary with a period less than 4 hours. The high temperature, coupled with high $\log g$, determined from the profiles of absorption lines, led all studies prior to Stasińska et al. (2009) to assume that the observed optical/UV component was the central star of the planetary nebula, i.e. the post-AGB star that lost its envelope and was the source of its ionization. Péquignot & Tsamis (2005) suggested that, if the ionizing star were even hotter, the deduced oxygen abundance could be increased to a more common level for oxygen-poor PNe. However, a higher temperature would have required a higher reddening to match the observed continuum slope, and Tovmassian et al. (2004) had already used a higher extinction than would normally be estimated for the direction of SBS 1150+599A in order to justify a temperature of 120 000 K .

Next, we obtained photometric light curves of the binary core of SBS 1150+599A (Napiwotzki et al. 2005). The orbital period of the system turned out to be 3.92 hr and, to explain the double-humped shape of the light curve, we were led to invoke a Roche lobe-filling optical/UV component. It was observed that the depths of the minima in the light curve are uneven, an effect known to occur when the visible component is irradiated by a hotter (more energetic) source. The orbital dynamics required that this invisible component be another compact object of at least 0.85 $M_\odot$ (Napiwotzki et al. 2005). Jacoby et al. (2002) pointed out the possibility that SBS 1150+599A may be associated with the X-ray source 1RXS J115327.2+593959. To detect the invisible source of irradiation and reveal the other component of the close binary, we observed it with the XMM-*Newton* X-ray observatory. We also conducted new optical spectroscopic observations of the object with the Gemini-North telescope to improve our knowledge of radial velocities of the optical/UV component of the binary and to better fit photospheric line profiles with atmospheric models. We also used the publicly available HST STIS observations of the object in the UV to bridge the optical and X-ray observations discussed here.

The ionization state and chemical composition of the planetary nebula are analyzed in a companion paper (Stasińska et al. 2009), while here we present a multifaceted analysis and modeling of the binary system. We analyze the history and the future of the stellar system in the light of evolutionary models for close binary stars.

In Section 2, we present our new observations; in Section 3 we determine the physical parameters of the binary; in Section 4 we discuss the evolution of the object from the early stages, when it was a wide system comprised of main sequence stars, to the latest stage of a merging of two white dwarfs (WD) with possible type Ia supernova outcome; and in Section 5 we summarize our main results.

2. Observations.

2.1. Optical observations.

A spectrum of TS 01, with an ample coverage of 3800–9200 Å is available in the Sloan Digital Sky Survey (SDSS[1]). It was taken on 2002 May 17 (spSpec-52411-0953-160). We used the newly calibrated spectrum that appears in the SDSS Data Release 7. This spectrum provides probably the best flux calibration, in a perfect agreement with HST spectra (see below).

The stellar absorption lines of the Balmer series

[1] http://www.sdss.org

and of He II are difficult to detect due to their shallowness, the faintness of the object (V$\sim 18^{\rm m}$), and the presence of very intense emission lines from the nebula. Only 7 spectra with measurable absorption features were available from our CFHT observations (Tovmassian et al. 2004). The short orbital period and consequent line smearing by the long exposures, and the necessity of relatively high resolution to effectively disentangle emission lines from absorption indicated the need for observations with a larger telescope.

We proposed to observe TS 01 for a total of 16 hours, covering four orbital periods, with Gemini-North telescope. The observations were scheduled for service mode in semester 2006A, but only 20% were completed. The available observations were performed in two sets: on 2006 May 16 UT, 8 spectra were obtained, and, on 2006 Jun 09, four more were added. The weather conditions during the observations were not ideal. The exposure times were 700 s, so, in total, only about 3/4 of the orbital period was covered with a resolution in phase of 5%. The GMOS spectrograph was used with the B1200+G5301 grating, leading to effective spectral resolution of 1.65 Å (FWHM) and a spectral coverage of 3800–5000 Å. We observed the Balmer series from H_β to the highest members (H_9) This spectral range also includes the He II 4686 Å line, detectable in both emission and absorption. Auxiliary images (biases, flatfields, arcs) were used to reduce the data using the procedures in *gemini* package within IRAF[2] and prescriptions provided by Gemini staff and fellow observers[3]. The standard star PG 1545+035, observed with the same instrumental configuration on 2006 Aug 30 in apparently better conditions, was used in an attempt at flux calibration. However, the result of this calibration was not satisfactory. Instead, we used the spectrum of TS 01 available in the Sloan Digital Sky Survey (SDSS) data base to correct the continuum. The *Gemini* spectra were corrected for orbital radial velocity shifts using the orbital solution described below and then co-added. Combining the 12 radial velocity (RV) shifted spectra allowed us to improve the profiles of stellar absorption lines and to get rid of nebular emission lines. The resulting spectrum, after 13 pixel boxcar smoothing, is presented in Fig. 1.

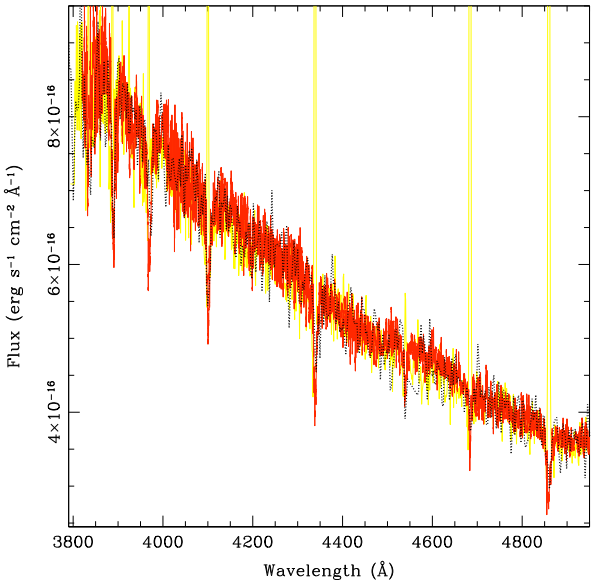

Fig. 1.— The stellar spectrum of TS 01 obtained at Gemini North (solid red line). The spectrum is a combination of 12 individual spectra, observed at different orbital phases, and smoothed with a 13 pixel boxcar. Before combining, the individual spectra were corrected for orbital motion. The SDSS spectrum, containing nebular lines, is plotted in yellow. The black dotted line is the single HST spectrum obtained for the same spectral range (see the text).

Previous observations of TS 01 are used here to analyze the nature of the stellar core. In addition to the above mentioned 7 CFHT spectra of lower spectral resolution, they include multiband photometric observations, briefly presented in Napiwotzki et al. (2005). They were obtained on two consecutive nights with the 2.2 m telescope at Calar Alto and the BUSCA CCD camera system that allows simultaneous direct imaging in four colors. The differential photometry was performed using comparison stars in the field of view. These photometric data were complemented by CCD photometry in the V filter obtained with the 2.1 m telescope at the Observatorio Astronómico Nacional in the Sierra de San Pedro Mártir (OAN SPM) on 2004 Apr 09. Additional photometric data were provided by the optical monitoring in-

[2]Copyright(c) 1986 Association of Universities for Research in Astronomy Inc.

[3]http://www.astro.caltech.edu/~kelle/gmos/gemini_reduction.html

strument (OM) on board XMM during the X-ray observations. Optical and UV data from direct images in the optical range as well as integrated flux from spectroscopic observations were also incorporated into the time series. For the time series analysis, the photometric data from the different wavelengths and bandpasses were normalized to a common mean value and combined.

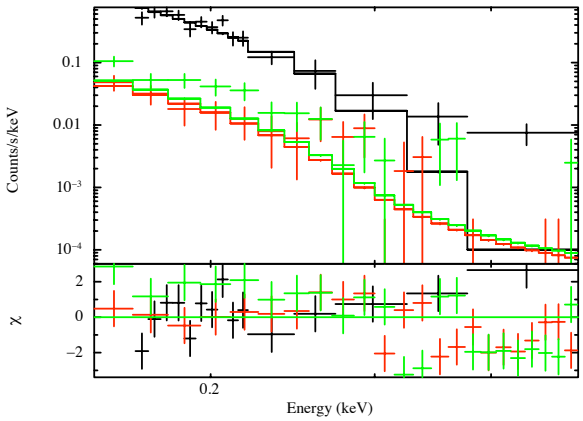

Fig. 2.— The source spectrum in all three detectors, PN, MOS1, and MOS2 (black, red and green crosses respectively) are fitted with the same black body model (lines of corresponding colors). The photons are concentrated in the lowest 0.1– 0.3 keV range. There is general consistency between all three EPIC detectors at energies below 300 eV. In the 0.4 – 0.5 keV bin, the counts start to differ, but the statistical significance of this is very low taking into account low count rates and calibration uncertainties.

2.2. Ultraviolet observations.

The first UV data for TS 01 were obtained in the far-UV using the *Far Ultraviolet Spectroscopic Explorer* satellite (FUSE). Details of these observations and their results are provided in Tovmassian et al. (2004).

Later, observations in the near-UV were obtained with the Hubble Space Telescope (HST) (Obs. ID 9466). In 2003 May, HST obtained spectra of TS 01 with the Space Telescope Imaging Spectrograph (STIS) in FUV, NUV, and CCD modes to cover the entire UV and optical. Continuous (uninterrupted by the Earth occultations) exposures with the G140L and G230L gratings were acquired. Five spectra with each grating and with individual exposure times of 4675 s and 2850 s, respectively, were acquired and combined to produce the final spectrum. One 600 s exposure was taken of the UV-optical spectrum (G430L grating) to connect the UV data with the optical. This last spectrum, as a result of its short exposure time, fails to reveal relatively weak, though important, emission lines in the optical UV, but provides a decent stellar spectrum that overlaps nicely with the NUV and SDSS spectra. This spectrum is also plotted in Fig. 1 and is in very good agreement regarding absorption features. The object was also observed in 2003 June with High Resolution Camera (HRC) of the Advanced Camera for Surveys (ACS) in the F334N & F658N filters to obtain images in the strong nebular lines of [Ne V] and H_α, respectively.

The pipeline-reduced STIS spectra were utilized to extract the stellar continuum. The integrated fluxes of individual exposures in UV range were also summed to produce a light curve in the UV range.

2.3. X-ray observations.

TS 01 was observed with XMM-*Newton* (obs-ID 0404220101) on 2006 Nov 01–02 (revolution 1263) in a continuous 27 ks exposure. The X-ray-counting EPIC instruments were operated with the thin filter in the PN small window mode and full window for the MOS detectors. The object was too faint for EPIC-RGS detectors. The optical monitor (OM) instrument on board XMM-*Newton* took 16 images in a *B* filter, each of 22 minutes duration. No pile-up was detected in either of the EPIC detectors. Background photon flares were detected during only 35-40% of exposure, mostly towards its end. The 7.5 hour exposure is just shy of two orbital periods (2×3.9 hours) of the binary system. The data from the first orbit were completely free from background flaring effects. The observed mean source count rates were 0.033 ± 0.002 in the PN, 0.0025 ± 0.0004 and 0.0053 ± 0.0005 cnts s^{-1}, in the MOS1 and MOS2, respectively.

The data were reduced using XMM-SAS (version 9.0). For the MOS detector, the source and background photons were extracted from a circular aperture and surrounding annulus correspondingly. For the PN detector, we tried subtraction

of background from 2 different circles near the source, since the small window did not allow to use a large annulus. We found no substantial differences in background removal from different areas. Events with detection patterns of up to quadruples were selected.

Background-subtracted spectra in the three EPIC detectors and a single blackbody model corresponding to each detector are shown in Fig.2. Estimates of the total galactic H I column density varies from $N_{\rm H} = 1.8 \times 10^{20}$ (Kalberla et al. 2005) to $N_{\rm H} = 1.53 \times 10^{20}{\rm cm}^{-2}$ (Dickey & Lockman 1990). The X-ray spectral analysis, with the column density fixed to the mean value determined for the direction of TS 01 ($N_{\rm H} = 1.6 \times 10^{20}{\rm cm}^{-2}$), gives a best fit for $kT = 17\,{\rm eV}$ (T$\approx$ 195 000 K). Based upon the XSPEC (Arnaud 1996) modeling, the 90% confidence region spans $kT = 12.7 - 18.0$ eV. The source is extremely soft and emits only in the narrow range spanning 100 – 300 eV. This range is notorious for its unreliable calibration (e.g. Mateos et al. (2009) for the latest evaluation) and routinely excluded by observers. However there is a good agreement between flux in the PN and MOS detectors for 0.1–0.3 keV (Fig. 2). Although the PN detector suggests the possibility that there is emission in excess of the blackbody in the 0.4-0.5 keV bin, the excess is not confirmed by either of the MOS detectors, making it unlikely that it is a real spectral feature. The analysis of ROSAT RASS archival data reveals that the source was poorly covered and the background is uneven, making spectral fitting useless, though it does confirm the extreme softness of the source.

In Fig. 3, the light curve of the source in the PN detector is presented extracted in two energy bands, 0.1-0.3 keV and 0.3-10 keV. This light curve demonstrates that practically all photons from the source are emitted in the narrow soft band, that the background flaring occurs mostly in the last quarter of the 27 ks exposure, and that the flares do not affect the soft band, where the source emits, but are rather strong in higher energies, confirming their nature as background. A similar picture emerges from the MOS detectors. However, we have chosen a conservative approach and excluded all episodes when the count-rate exceeded 0.1 counts/s from the analysis of the source in all three detectors.

The X-ray light curve of the source in the PN detector shows some flickering but no definite periodic variability. There is no correlation between the power spectra obtained for the three different detectors and the optical light curve.

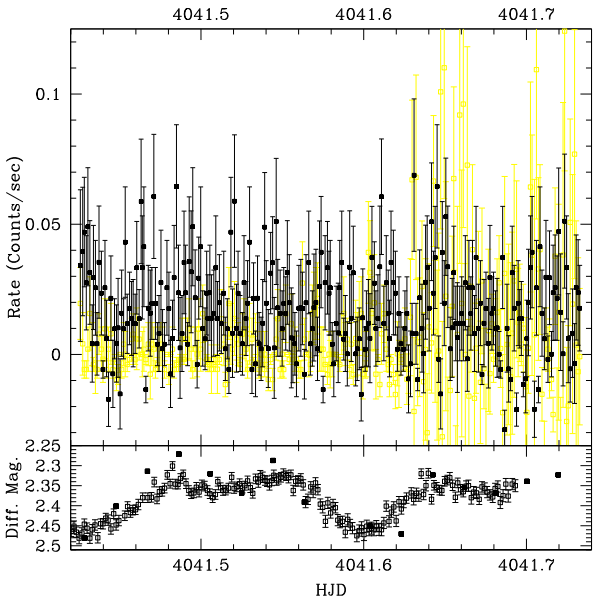

Fig. 3.— The X-ray light curve of the source in the PN detector (top panel). The filled symbols represent the light curve in 0.1–0.3 keV range, while the open symbols (yellow) are the counts in the 0.3–10.0 keV band. The count rate above 0.3 keV is practically zero, except during the final part of the exposure, where they are dominated by background flaring. In the extreme soft band, 0.1–0.3 keV, the count rate is approximately constant (0.033 cnts/sec) for the entire duration of the observation. The bottom panel displays the optical light curve for comparison. Black points are OM measurements on board of *XMM-Newton* at the time of the observations whereas the open boxes are V light curve obtained at SPM (2.5 years earlier; shifted in time according to phases).

The OM measurements in the B filter from the pipeline reduction were simply transformed into a magnitude scale by taking the logarithm and shifted to the same average value as the ground-based optical differential photometry. In this way, they were used to identify the precise orbital phasing for the X-ray data.

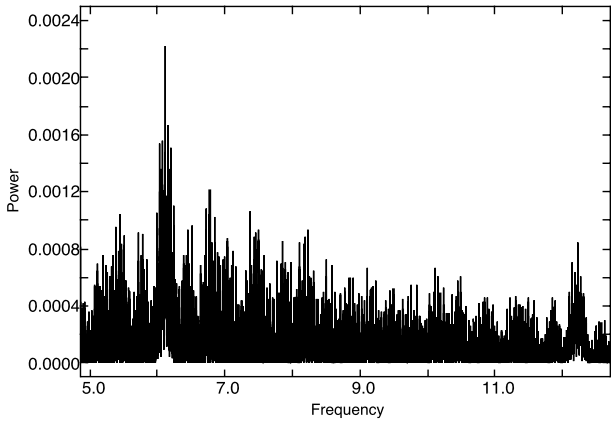

Fig. 4.— The power spectrum of all photometric data. The strongest, single peaked maximum corresponds to the orbital period, at $6.1159\,\mathrm{day}^{-1}$. The first harmonic, at $\approx 12\,\mathrm{days}^{-1}$, is also prominent in the power spectrum because of the double-humped nature of the light curve.

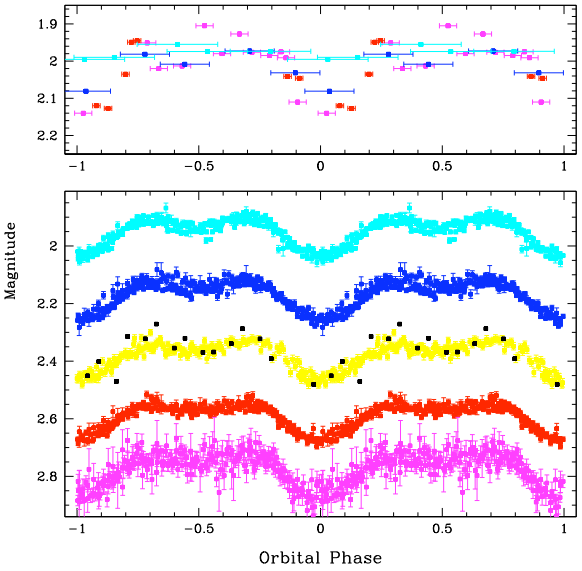

Fig. 5.— The light curve of TS 01 folded with the orbital period. The lower panel presents optical light curves. From top to to bottom are: BUSCA UV and B, Johnson V from SPM, XMM OM (black points), and finally BUSCA R and NIR. The upper panel presents HST data: H_α (red), [Ne V] (magenta), the integrated spectral flux in the NUV (dark blue) and FUV (cyan). The horizontal error bars in the upper panel denote the exposure time converted to orbital phase.

3. Physical parameters of the close binary.

3.1. Orbital Period.

The orbital parameters were roughly determined with the discovery of the binarity (Tovmassian et al. 2004). However the precise orbital period can be determined only with the accumulation of enough data over a sufficiently long period of time. At the moment, we have uneven temporal coverage spanning about 1000 days, combining multicolor photometry from the ground, optical monitoring on board of XMM-*Newton* and narrow-band photometry from HST in the optical range. We also considered the integrated flux in narrow bands from UV spectra obtained with HST. All of the photometric data were shifted to an arbitrary mean magnitude and analyzed for the presence of a period using the discrete Fourier transform (DFT) method. The power spectrum is presented in Fig. 4 with its strongest peak at 6.1159 cycles/day, the frequency corresponding to the orbital period, and its $2f$ alias at 12.23 cycles/day. The resulting ephemeris is

$$\mathrm{HJD} = 2452760.6756(5) + 0\overset{\mathrm{d}}{.}163508(3) \times \mathrm{E},$$

where the zero point T_0 corresponds to the deeper minimum in the light curve. The light curves of TS 01 folded with the estimated 3.924 h orbital period are presented in Fig. 5 in different bands. In the bottom panel multi color photometry from Calar Alto is plotted combined with V band data from OAN SPM and OM-XMM. In the top panel the measurements from a variety of HST detectors are displayed. Even though the HST data in the optical narrow filters F334N & F658N include large contributions from the nebular emission lines, they nevertheless show variability of the stellar core with a similar amplitude as in the broad-band filters. The UV light curves have the same double-humped shape as their optical counterparts, but the amplitude decreases as the wavelength moves further into UV. The far UV observations with the G140L grating have exposures that are almost a quarter of the orbital period, so orbital smearing is severe. Degrading the optical light curves to a similar time resolu-

tion shows that the small amplitude in the far UV light curve is the result of smearing rather than an actual change in the amplitude of the variation.

The possible interpretation of the double humped light curve was briefly discussed in Napiwotzki et al. (2005). With the X-ray observations in hand we are now confident that the double hump is a result of the surface projection of the ellipsoidal binary component that fills its Roche lobe and orbits its more massive companion on a relatively high-inclination orbital plane (to the line of sight), coupled with the effect of gravitational darkening. The difference in minima dips, on the other hand, is the consequence of the heating of the surface of the Roche lobe-filling star that faces a hotter, but much more compact companion. This phenomenon is often observed in compact binaries. It is also referred to as reflection (Wilson & Devinney 1971). In what follows, we

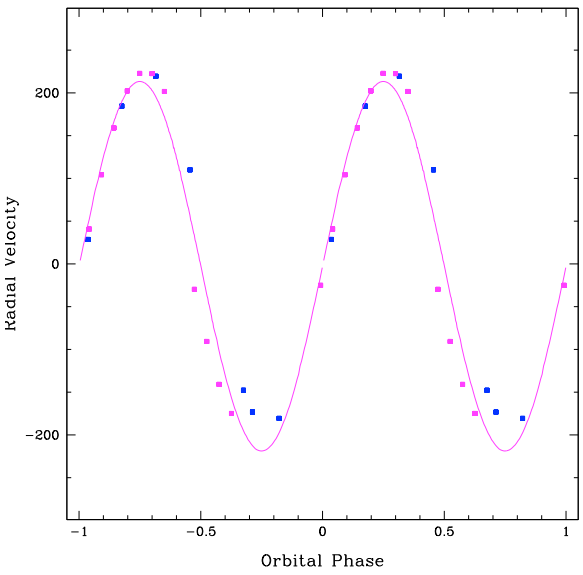

Fig. 6.— The radial velocity curve of TS 01 folded with the orbital period. The points marked in magenta are measurements from *Gemini* spectra. The CFHT points are presented in blue. The latter were measured anew with the same parameters deduced from the line profile fitting by FITSB2. The *sin* fit to the data presented here is practically indistinguishable from RV curve calculated by *Nightfall* (see below).

qualify by *cool* or *optical* the Roche lobe-filling component, since it is the main contributor of light in the optical range, and by *hot* or *X* the hotter component which irradiates its cooler companion. We refrain from the usual wording of primary and secondary components in this paper, since, as we later discuss, the roles of primary and secondary changed during the evolution of this system.

The optical spectra are too sparse to determine the orbital period independently, but they cover almost all orbital phases. The orbital period estimate from the photometry is good enough to calculate the orbital phases for the spectra. Therefore, by measuring the radial velocities of the absorption features in each spectrum, we are able to construct the radial velocity curve. We used the FITSB2 procedure to measure the RV of absorption features. FITSB2 performs a simultaneous fit of the spectra covering different orbital phases, i.e., all available information is combined into the parameter determination procedure (Napiwotzki et al. 2004). The fit results are the stellar parameters as well as the RVs (Napiwotzki et al. 2004). We followed the same procedure as Tovmassian et al. (2004) adding the new *Gemini* spectra. However, here, we sought solutions with relatively low temperatures, because we now had a better idea of the temperature composition of the binary (Tovmassian et al. 2007). The best fits were achieved with $T_{\rm eff} = 60\,000 \pm 5\,000$ K, $\log g = 5.17 \pm 0.07$

The radial velocity (RV) curve presented in Fig. 6 is fitted with a simple sinusoid. The phase zero corresponding to the -/+ crossing of the RV curve coincides with the deeper minimum in the light curve. It confirms our interpretation that, at phase 0.0, the *optical* component is seen in conjunction from behind, turning to the observer its smallest projected area and coolest surface temperature. At phase 0.5, the *optical* component is seen with the same projected area, but presents the face with the highest temperature, as result of the intense heating from the *X* component. A formal orbital solution leads to semi-amplitude of RV $K_{\rm cool} = 216 \pm 10$ km s^{-1}, and systematic velocity of the system $\gamma = 0 \pm 12$ km s^{-1} relative to the nebular emission lines.

The correct determination of phases and RVs allowed us to combine all 12 *Gemini* spectra, eliminating the nebular emission line components, and delineating the absorption profiles with increased

signal-to-noise. The co-added spectrum is shown in Fig. 1. In combination with the UV stellar spectra from the HST observations, where the stellar component is easily separated from the nebular one due to the high spatial resolution, the coadded spectrum allows us to perform a model atmosphere analysis of the cool component (see Sect. 3.2.

3.2. Temperatures and Radii.

TS 01 is clearly the first planetary nebula known to contain a double-degenerate binary (De Marco et al. 2008). The first indication that the previous interpretations (Tovmassian et al. 2004; Péquignot & Tsamis 2005) of the central star of TS 01 may be incorrect came from the shape of its light curve (Napiwotzki et al. 2005). Now, armed with the X-ray data, we know that even a 130 kK star can not produce the observed X-ray flux and that an additional component is required to explain the observed spectral energy distribution (SED).

We analyze the SED, fitting it with a blackbody as a first approximation. The actual atmosphere can be significantly different from a black body at wavelengths shorter than 900 Å, but as starting point a black body gives us a good idea of what we are dealing with. We will discuss deviations from blackbody later in the paper. The data were de-redden according to Schlegel et al. (1998) with a canonical ratio of total-to-selective absorption, $E(B-V) = 0.03$ mag and $R_V = 3.1$. We simultaneously fit two black bodies to the observed spectral energy distribution by introducing best guesses for T_{cool}, T_{hot}, r_{cool}/D, and r_{hot}/D, where D is the distance to the object, and calculating their best fit values. Since there is a gap between extreme UV and X-ray wavelength ranges, and since the slope of the X-ray data is not strictly that of a black body, we obtain three distinct solutions with similar χ^2 by varying the input parameters. Possible solutions are presented in Table 1.

The resulting fits are presented in Fig. 7. The black body solution for the *hot* component is $T_{hot} \approx 180,000 \pm 25\,000$ K. Minimum $\chi^2 \approx 2.6$ can be achieved with significantly different temperatures for the *hot* component, depending upon which part of X-ray data the fit relies on. But the hot solutions with $T_{hot} \geq 175\,000$ K, marked in the Fig. 7 as shaded area, do not work, as can be seen below, because only certain ratios between the *hot* and *cool* components fluxes can produce the required difference in the depths of minima of the light curve. To restrict the range of possible solutions, we analyze the form of the light curve, together with the radial velocity curve, using the binary star modeling code *Nightfall* [4].

Nightfall is based on a physical model that takes into account the non-spherical shape of stars in close binary systems, as well as the mutual irradiation of both stars, and a number of additional physical effects such as gravitational darkening and albedo. We fitted simultaneously the light curves in three bands and the radial velocity curve. The program uses differential magnitudes and is tailored to the Johnson photometric system. Taking into account that the shape and range of amplitudes of the light curve is (a) similar in the BUSCA narrow filters and the Johnson V filter and (b) does not show large wavelength dependence in the optical range, we assigned BUSCA *uv* to the *U* filter, *b* to the *B* filter, and *r* to the *R* filter. We did not use *nir* band data, since it was the noisiest and would not add anything substantial to the analysis. We searched for solutions by setting the temperatures to the values estimated from the SED. We also fixed the total mass of the system close to the Chandrasekhar limit of 1.39 $M_\odot$. The real M_{tot} might be slightly lower or higher, that would not affect this analysis. Leaving the total mass parameter free, *Nightfall* tends to solutions involving massive stars, which are excluded. However, limiting the total mass still results in a variety of remaining parameters that achieve similarly good fits. The inclination angle of orbital plane to the line of sight, i, must be relatively high to produce the observed light variation due to the ellipsoidal form of the *cool* component, but not too high to produce eclipses, which we do not observe, neither in the optical, nor in X-rays. Inclination angles ranging from the high 40's to the low 70 degrees are acceptable, and the light curve form depends weakly on i within that range. The essential parameters for which we seek solutions are the masses and radii of the binary components. However, the RV and light curves fitting does not provide any clue on masses, so additional constrains

[4] http://www.hs.uni-hamburg.de/DE/Ins/Per/Wichmann/Nightfall.html.

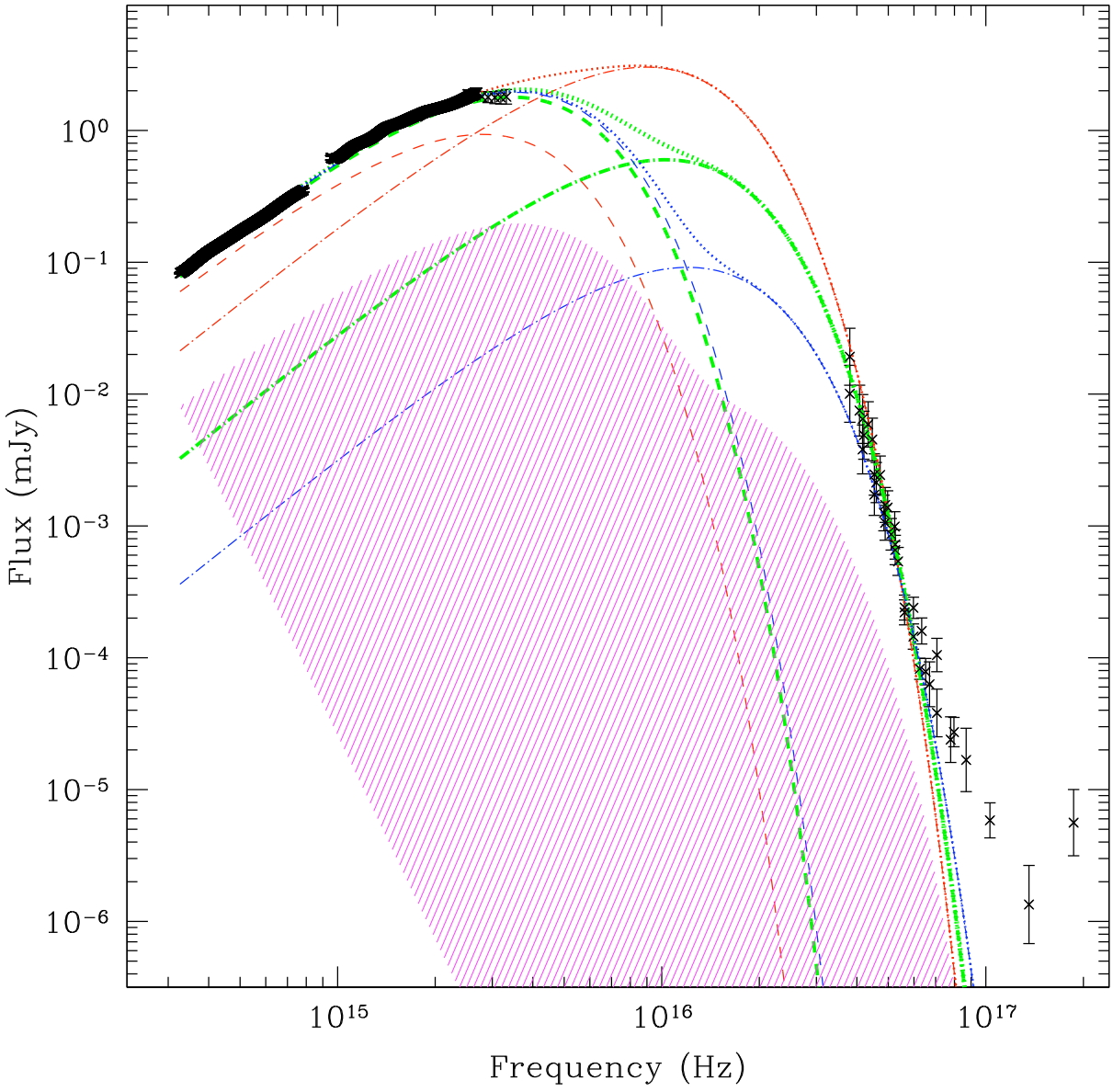

Fig. 7.— The spectral energy distribution (SED) of TS 01. The observed spectra are presented by crosses with error bars (SDSS + HST/STIS + FUSE+XMM). The observations are fitted with two blackbodies. Three pairs of blackbody solutions are presented according to Table 1. Dashed, dashed-dotted and dotted lines represent the *cool*, the *hot* components and their sum respectively. Shaded is the area in which the the radius of *hot* component determined from the light curve analysis starts to deviate from the one required for SED fitting. In this area the luminosity of *hot* component does not provide enough irradiation to the *cool* component to produce observed light curve. Thus, only a cool $\sim 160\,000$ K solution is viable.

Table 1: Output parameters of double black-body fits to the SED.

Solution	optical component T K	R/D $\times 10^{-13}$	D^a kpc	X component T K	R/D $\times 10^{-13}$	R^a $R_\odot$	log L^a $L_\odot$	χ^2
Cool	47 700	3.80	21.7	152 600	1.20	0.12	3.81	2.54
Intermediate	58 900	3.83	21.6	174 600	0.43	0.04	3.14	2.63
Hot	60 600	3.83	21.5	205 200	0.15	0.014	2.51	2.65

[a]The values of these columns were calculated assuming $R_{cool} = 0.43 R_\odot$, and corrected by a factor $D \sim \sqrt{F} = 0.85$ because the model atmosphere flux $F_{atm} \approx 0.73 \times F_{BB}$ with $T = T_{eff}$ at the optical wavelengths, as it follows from the analysis below (see 3.2.1 and 3.2.2).

were necessary.

3.2.1. The cool component.

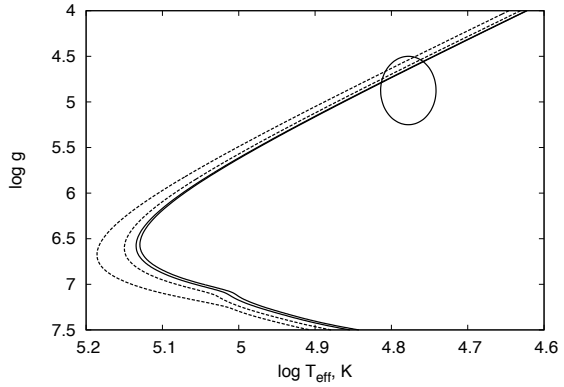

Fig. 8.— $T_{\rm eff}$- $\log g$ dependence for post-AGB models (Weiss & Ferguson 2009, and priv. comm.) Solid line - Z=0.004 for 0.529 & 0.533 $M_\odot$. Dashed line - Z=0.0005; 0.539, 0.551 $M_\odot$ correspondingly. Tracks for more massive stars spread out toward hotter temperatures. The ellipse indicates range of possible solutions for TS 01 stemming from variety of methods used in this paper.

The first estimate of the mass of *cool* component (Tovmassian et al. 2008, 2007) based on $T_{\rm eff}$ and evolutionary tracks for solar composition post-AGB stars from (Schoenberner 1983; Bloecker 1995) led to $M_{cool} \approx 0.58\,M_\odot$. Recent models for different metallicities (Weiss & Ferguson 2009) suggest $0.52\,M_\odot$ as the lower limit of the mass of a star that heats up to $\sim 60\,000$ K (see Fig. 8). For Z=0.001, the mass limit is actually $0.54\,M_\odot$. Fixing the mass of the *cool* component in *Nightfall* to that value, we find that regardless of other poorly-constrained parameters of the *hot* component, the *cool* star must have a radius of at least $0.42\,R_\odot$ to fill its Roche lobe up to 94-99% in order to produce the observed light curve. Since the cool component is ellipsoidal in shape, this radius, as determined by *Nightfall*, represents the mean radius. In fact, the radius depends only weakly on the mass adopted for the star, and is a stronger function of the binary system's mass ratio, which determines the size of Roche lobe. For range of mass ratios stemming from the total mass of the system in 1.3–1.45 $M_\odot$ interval the mean radius of the *cool* component lies within 0.42–0.45 $R_\odot$ range.

The mass and radius obtained for the *cool* component leads to a mean $\log g$ of 5.03 ± 0.03, a value deduced by averaging the unevenly distributed gravitational acceleration on its surface (Djurasevic 1992). A very similar value of surface gravity is obtained by using FITSB2 (§3.1).

Next, we modeled the stellar atmosphere of the *cool* component using the Tubingen NLTE Model-Atmosphere Package (TMAP)[5] (Werner et al. 2003; Rauch & Deetjen 2003). This code computes plane-parallel or spherical Non-LTE model atmospheres in radiative and hydrostatic equilibrium and considers opacities of all species from hydrogen to nickel. The determination of $T_{\rm cool}$ is based on the evaluation of the ionization equilibrium through the C III λ 1175 Å / C IV λ 1169 Å stellar absorption line ratio. We find $T_{\rm cool} = 55 \pm 5$ kK. At such a temperature, a surface grav-

[5]http://astro.uni-tuebingen.de/~rauch/TMAP/TMAP.html

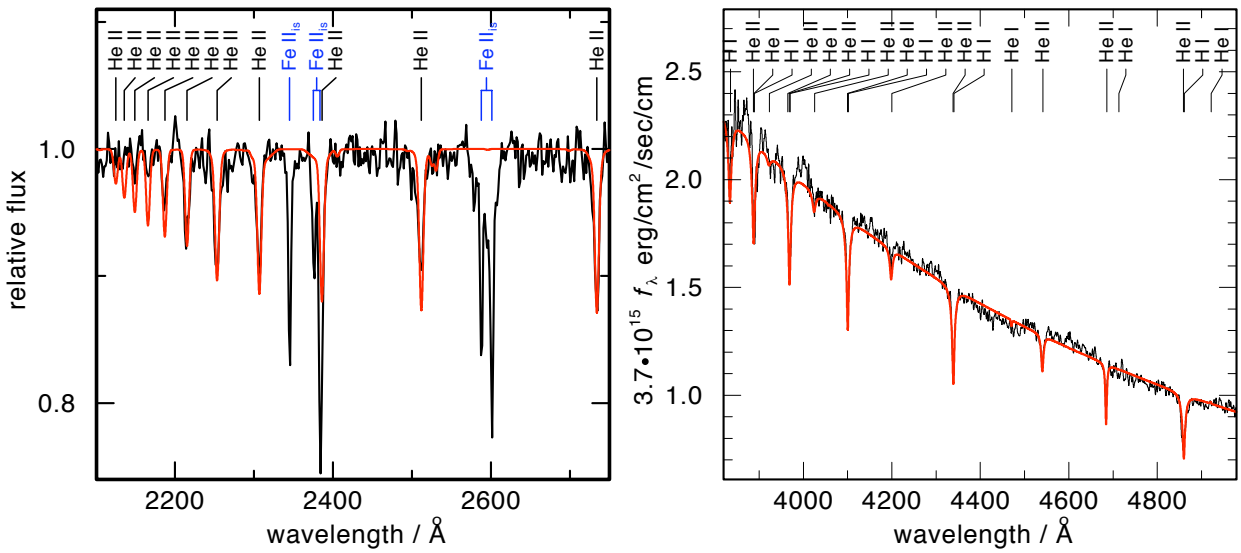

Fig. 9.— Comparison of a *TMAP* SED with observation. a. the STIS NUV range. The He II Fowler series (marked at top) are well reproduced; "is" denotes interstellar lines. b. the GEMINI North optical range. The H and He lines are marked at top.

ity of $\log g_{\rm cool} = 4.9 \pm 0.5$ gives a good agreement with the observed spectral line profiles (see Figs. 9 a & b, comparing a *TMAP* model with the *STIS NUV* observations and with the *gemini* spectrum, respectively). $T_{\rm cool}$ and $\log g_{\rm cool}$ cannot be better constrained given the quality of the data. However, the agreement between the values derived with *TMAP* and those derived with *FITSB2* and *Nightfall* confirms our correct assessment of the basic parameters of the *cool* component.

We performed some *TMAP* test calculations in order to derive upper abundance limits for some metals. These are summarized in Tab. 2. Note that the resonance lines of C IV and N V were not used in our abundance determination, since they were found to be affected by interstellar line absorption. The chemical composition of the *cool* stellar component is close to that of the nebula (Stasińska et al. 2009).

In Fig. 10, the model is compared with observations, covering continuously the whole range from 900 to 10 000 Å. Apart from the observations and atmospheric model, the nebular emission is shown as deduced in Stasińska et al. (2009), and the black body curves as implemented in *Nightfall*. The black body corresponding to the *cool* and *hot* components are denoted by open stars (red and blue

Table 2: Photospheric abundances of the *cool* component of TS 01. Ca-Ni are represented by a generic model atom. The errors for H, He, and C are about 0.3 dex. For N, O, Si, and the iron-group elements upper limits are given.

element	mass fraction
H	7.471E-01
He	2.525E-01
C	1.335E-04
N	< 8.306E-05
O	< 7.116E-05
Si	< 6.737E-05
Ca-Ni	< 1.319E-06

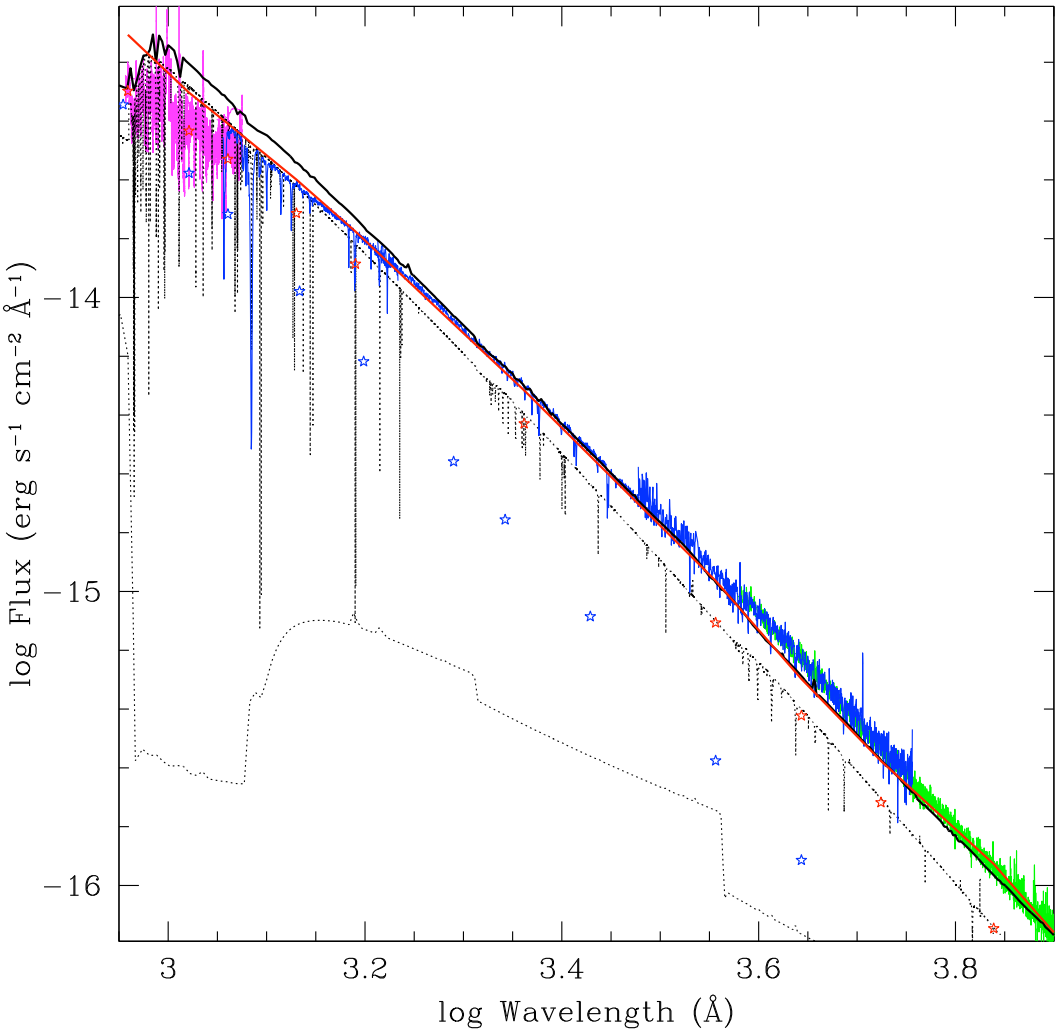

Fig. 10.— The spectrum of TS 01 from the far UV to the near IR. The observational data after extinction correction and nebular emission lines removal are denoted as follows: FUSE - magenta; HST (FUV +NUV+UVopt) - blue; SDSS - green. The models for the nebular and stellar emission are shown by grey dotted lines. The thick black line is the sum of the model continuum emission from the nebular and stellar components. The black-body solutions are presented by red open stars for the *cool* component and by blue stars for the *hot* component. The thick red line is sum of *hot* (162 kK) and *cool* ($\sim$ 57 kK) blackbodies plus nebular emission.

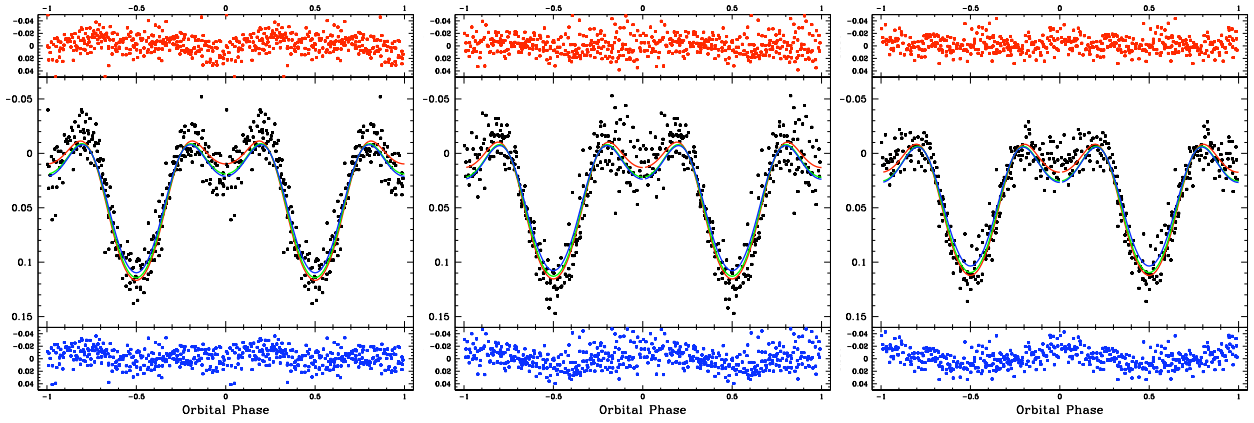

Fig. 11.— From left to right, the *Nightfall* fits to the light curves in *uv*, *b*, and *r*. In the main panel, the red, green, and blue curves represent the solution for X-component with $T_{\rm eff}$ of 162 kK, 182 kK, and 202 kK, respectively. The deviations with respect to the coolest and hottest solutions are shown in top and bottom panels, respectively. The complete set of parameters used in fitting is given in Table 3. The simultaneous fit to the RV curve is similar to the *sin* curve presented in Fig. 6.

respectively). The sum of the two black bodies and the nebular continuum within the observing slit as computed in Stasińska et al. (2009) is represented with the thick red line in Fig. 10. The fit of the models to the observations is excellent from the near infrared to 1500 Å.

The curve representing the stellar model plus the nebular emission departs slightly from the observations at shorter wavelengths. The problem with the flux above 1500 Å in the NLTE models has been noted before (Rauch 2008). More importantly, the model is calculated for a spherically symmetric star with a homogeneous temperature distribution over its surface. However, we know that the *cool* component is strongly irradiated and gravitationally distorted, which affect both its SED and the gravitational acceleration over the surface of the star. We approximate the observed, phase-averaged spectrum by the non-irradiated atmosphere model even though, in some orbital phases, we observe the irradiated hemisphere of the *cool* component. The spectra of irradiated atmospheres are flatter in the far UV in comparison with the spectra of non-irradiated atmospheres with the same $T_{\rm eff}$ (see next subsection). Therefore, the average flux in the far UV decreases in comparison of the non-irradiated atmosphere spectrum. Overall, we have very good agreement between models and observations.

3.2.2. The hot component.

The parameters of the *hot* component are less certain. Our knowledge of the *hot* component is based on the binary period, the fact that the *cool* component is partially irradiated to produce the observed light curve, and the X-ray flux, which cannot originate from the *cool* component. There is an extensive argument in Napiwotzki et al. (2005) discussing why the *hot* component should be a compact object with a mass exceeding the mass of the *cool* component. However, neither the light curve, nor the X-ray spectra allow us to determine the temperature or radius of the *hot* component as well as we did for the *cool* component.

We face two problems in the case of TS 01's *hot component*. First, TS 01 is only detected in short, soft end of the X-ray range. Second, the calibration of data at the extreme soft end of the XMM-*Newton* spectral range is not very reliable. Both prevent us from fitting exact atmospheric models to it. Hence, like most studies of supersoft X-ray sources, we are forced to continue the analysis using the blackbody that successfully describes the spectrum of the *hot* component in the optical and UV range up to 4×10^{15} Hz (see Fig. 7). We also note that this introduces an overestimate of

Table 3: Parameters of *Nightfall* fits.

	opt/UV component					X component				
Solution	T	M	R	log g	inc	T	M	R	log g	χ^2
	K	$M_\odot$	$R_\odot$		deg	K	$M_\odot$	$R_\odot$		
Cool	57 100	0.537	0.44	5.02	52.8	162 195	0.853	0.135	6.1	46.27
Intermediate	57 264	0.537	0.43	5.04	53.0	182 195	0.853	0.113	6.3	46.37
Hot	57 104	0.537	0.43	5.04	53.2	202 000	0.853	0.088	6.5	46.43

the luminosity of the X-ray source (Heise et al. 1994; Swartz et al. 2002). On the other hand the temperature can be either overestimated (Swartz et al. 2002), or underestimated (Heise et al. 1994; Ibragimov et al. 2003). Therefore, when estimating the temperature of the *hot* component in the optical/UV range separately from estimates in X-rays, we should not worry too much if discrepancies arise. It is within the optical/UV range that the irradiation of the *cool* component matters, so we may fix the parameters of the *cool* component in *Nightfall* and seek solutions for the *hot* component. Even so, varying freely both the radius and temperature of *hot* component, we still do not reach unambiguous solutions.

In Fig. 11, we present the fits produced by *Nightfall* to light curves in three different filters. The parameters for the fits for the different temperatures of the *hot* component are presented in Table 3. The temperature and the mass of the *cool* component were kept fixed (the difference in mean temperatures of the *cool* component in the Table reflects the different degree of irradiation). The parameters that were fitted are the orbital inclination angle, the fraction to which both components fill their Roche lobes, and the temperature of the *hot* component. Three models with different temperatures for the *hot* component are displayed in Fig. 11. The fits shown red, green, and blue correspond to T_{hot}= 162, 182, and 202 kK, respectively. The lower and upper panels show the deviations of the fit from the observations for the extreme cold and hot solutions. As can be seen from Fig. 11 and Table 3 the differences between three models ranging from 160 to 200 kK are not important in the optical domain.

Note, that the range of temperatures for *hot* components obtained from blackbody fitting to SED and from the fitting of light curves by *Nightfall* are similar. But comparison of Tables 1 and 3 shows that only for low temperature solution the radii deduced by both methods are compatible. Introducing the radius of the *cool* component deduced from *Nightfall* into the R_{cool}/D parameter used in the fit of two black bodies to the SED results in a distance of 25 kpc for the minimum radius of R_{cool} = 0.42 $R_\odot$ and leads to $R_{\rm hot} \approx 0.13 R_\odot$ for a blackbody temperature 150 kK. The color temperature of the *hot* component is probably slightly higher. This is caused by the divergence of the real atmosphere from the black-body at high energies and also by the use of a Roche lobe-shaped *cool* component in *Nightfall*, instead of the spherical shape in all other calculations. Similarly, using stellar atmospheres instead of black-bodies reduces the distance to about 21 kpc, as reflected in Table 1. Increasing temperature is compensated naturally by a smaller radius. The solutions with temperatures above 175 kK come up with parameter R_{hot}/D too small to be compatible with results of light curve fitting. In Fig. 7 the blackbody solutions of *hot* component that fall into shaded area are not luminous enough to provide necessary irradiation and produce the observed light curves. In the meantime, temperatures above 185 kK are not tolerated by ionization modeling of the nebula (Stasińska et al. 2009).

Therefore, we consider 160–175 kK temperature range and $R_{hot} \approx 0.1 R_\odot$ to be the closest to the real properties of the *hot* component. Note that the *hot* component has a radius $R_{hot} \geq 0.04 R_\odot$ at least. This is much larger than an ordinary white dwarf. As such TS 01's *hot* component is very similar to the supersoft X-ray source (SSS) Lin 358, one of the two SMC symbiotic stars studied by Orio et al. (2007). Majority of estimates of temperatures and luminosities of super-soft X-ray sources are made using black bodies and values obtained here are useful when comparing to other similar objects.

Fitting an exact atmospheric model to the X-ray data for the *hot* component does not make

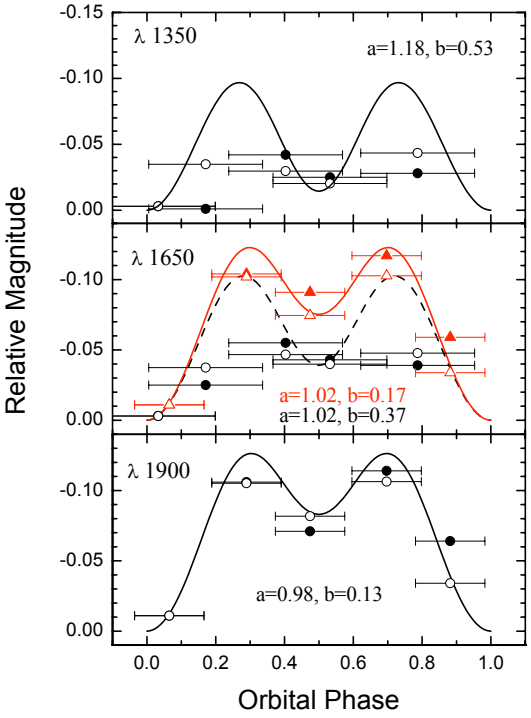

Fig. 12.— Comparison of the observed light curves (filled symbols) at λ1350 Å (top panel), λ1650 Å (middle panel), and λ1900 Å (bottom panel) with the computed light curves in the same bands (solid and dashed lines). The horizontal error bars mark exposure length for each point. The light curves at λ1650 Å are obtained separately from *HST* FUV (circles) and NUV (triangles) detectors. Their disparity indicates the difference of light curve smoothing due to the exposure length. The model fluxes, integrated in the same phase ranges as observed ones are shown by open symbols. All models are computed for the *cool* solution from Table 2. To account for differences between the black body and real atmosphere we introduced the parameters a & b (see text), obtained empirically from comparison of these two observed light curves.The values of parameters for flux correction in corresponding bands are marked in the plot.

much sense, because the observed energy range is too small and the quality of the data is too poor.[6]

An additional test for checking the estimated temperature of the *hot* component comes from modeling of the light curve in the UV. However, *Nightfall* cannot calculate model fluxes in the UV, so we implemented our own code (Shimansky et al. 2002), which calculates the irradiation in a binary according to the prescription in Howarth & Wilson (1983). *Nightfall* is based on the same algorithm, so we naturally obtained exactly the same light curves for optical bands. We compute the UV light curves for the cool soloution from Table 3, and present it, together with the observed one, in Fig. 12. In computing the UV light curves we take into account the difference between a black body and a stellar atmosphere introducing the ratio $f_\lambda = F_\lambda(\mathrm{BB})/F_\lambda(\mathrm{BSA})$ of black body and a stellar atmosphere fluxes at a given wavelength[7].

3.3. The total mass.

The mass of the *hot* component cannot be determined directly from the observed data. However, simultaneously fitting the RV curve and light curves indicates a tendency towards improvement as the total mass approaches the Chandrasekhar limit. In Fig. 13, we plot the calculated χ^2 as a function of the total mass of the system, by fixing in *Nightfall* the temperatures of the components to our best estimates, i.e. 57 and 162 kK and adopting a mass of $0.54\mathrm{M}_\odot$ for the *cool* component. The lower limit for total mass is of $1.25\,\mathrm{M}_\odot$, corresponding to a *hot* component with a mass of $\sim 0.7\,\mathrm{M}_\odot$. This mass corresponds to the lower limit for a white dwarf to sustain steady nuclear

[6]For the analysis of the ionization of the nebula, however, using a black body would cause serious problems at high energies. This is why, for their photoionization modelling, Stasińska et al. (2009) selected a suitable spectrum from a grid of models with halo composition, which reasonably well describes the observed fluxes both in opt/UV and X-ray range and provides a more realistic picture.

[7]In the optical part of the spectrum $f_{\mathrm{opt}} \approx 0.73$ for both the *cool* and *hot* components; near the Lyman edge the SED of the *cool* component is different from a blackbody: $f_{1350} \approx 1.18$ and $f_{1650} \approx 1.02$; the values of f_λ for the *hot* component remain close to 0.73. Moreover, the values of f_λ for the *cool* component must depend on the irradiation flux. If the irradiation flux increases, f_λ decreases, because the spectra of the irradiated stellar atmosphere are getting closer to a black body spectrum. The best approximation of the observed light curves by the model light curves was obtained for a simple linear dependence $f_\lambda = a - b\cdot(F_{\mathrm{irr}}/F_0)$, where F_{irr} is the irradiation flux at a given point of the *cool* component surface, and F_0 is the flux from the *cool* component at the same point. A change of the continuum slope in the UV band at the various orbital phases, observed by HST, confirms this picture. Parameters a and b deduced for each λ are presented in Fig. 12.

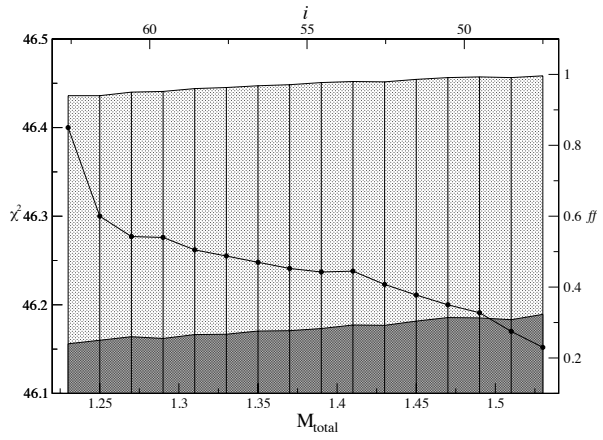

Fig. 13.— The line with dots depicts the dependence of the χ^2 value on the total mass of the system. Fixed parameters in the calculations were the temperatures of the components (55 & 160 kK respectively) and M_{cool} (0.54 $M_\odot$). The free parameters were the inclination of the binary orbit i, which changed similar to the χ^2 in a range of values shown on the upper axes; and the Roche lobe filling factors (ff) of both components shown as shaded areas in a range of values marked on the right side axes. The dark shaded area corresponds to Roche lobe filling factor of the *hot* component and the light grey to that of the *cool component*.

burning on its surface. Increasing the total mass of the binary from that minimum value produces a decrease in the χ^2 value, with a small plateau of χ^2 at about $1.4M_\odot$. The χ^2 keeps falling as the total mass increases. This is due to the fact that rising mass of the *hot* component shrinks the Roche lobe of the *cool* star. At around $M_{total} = 1.47$ the *cool* component fills its corresponding Roche lobe to 99.9%, which helps a better fitting of the light curves. Improvement of χ^2 from there on is conditioned by the rapid increase of size (Roche lobe filling factor = ff) of the *hot* component, which might be unrealistic. The mass could in principle be constrained by the fit to the RV curve, but unfortunately the RV data is too poor in quantity and quality to have strong influence on χ^2. We consider the flattening of the $\chi^2 - M_{total}$ curve around $M_{total} = 1.40$ as an indication of the best solution, where a balance is achieved between fitting the light and RV curves at the same time, but of course a lower than Chandrasekhar limit mass is not excluded. Better measurements of radial velocities are required for a more reliable determination of stellar masses in TS 01.

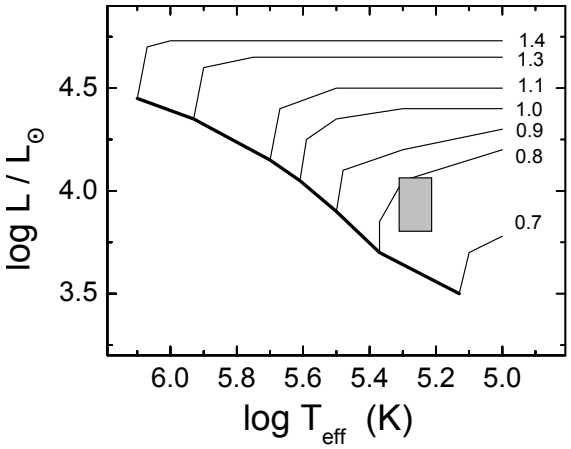

Fig. 14.— Position of the *hot* component in the temperature-luminosity diagram (filled box) respective to the tracks of hot accreting white dwarfs in the steady-burning approximation (Iben 1982). The bold solid curve shows the high-temperature boundary of the stable-burning strip. The numbers by the tracks are corresponding white dwarf masses in $M_\odot$.

The mass estimate of the *hot* component can be checked from its position in the H-R diagram (Suleimanov & Ibragimov 2003). Figure 14 shows position of the *hot* component of TS01 in the log T_{eff} − log L diagram. It suggests that the object has a mass of about $0.78 \pm 0.02\,M_\odot$, if it has not cooled much since active intense accretion ceased. The lower luminosity boundary of the rectangle corresponds to the upper luminosity limit obtained from the SED, while the upper luminosity boundary corresponds to the luminosity, obtained from the optical light curves modeling. Given all uncertainties, the agreement with mass estimate obtained above seems to be rather good. But we note cautionary that the tracks were calculated assuming solar chemical composition of accreted matter, while real chemical composition of the *hot* component is not known and that the structure of its envelope, which defines the rate of cooling, may be different from the one of a steady-

burning object.

For the readers convenience we summarize parameters of the binary estimated by variety of methods in Table 4.

4. Evolutionary considerations.

4.1. Formation of TS 01

Below, we present examples of evolutionary scenarios that can result in the formation of a system reasonably similar to TS 01. These scenarios envision the formation of a massive white dwarf that cools for a long time but is reheated by compression due to accretion and nuclear burning of material captured from the stellar wind of companion. The core of the latter is currently the less massive component of the binary nucleus of TS 01. In the analysis of the origin of TS 01, one has to take into account its location in the Galactic halo, where star formation ceased about 10 Gyr ago (e. g. Marín-Franch et al. 2009). This sets an upper limit of $< 1\,\mathrm{M}_\odot$ for the mass of the progenitor of the *cool* component.

The presence of an old white dwarf and a nascent white dwarf in a system with an orbital period of 3.92 hr only implies that previous evolution of the system involved common envelope(s). First, let us assume that both components of the nucleus of TS 01 had AGB precursors. This suggests the following scenario[8]. The initial masses of the components are significantly different. The initial system is so wide that the primary evolves to the AGB unaffected by the presence of the companion. In the FGB[9] and AGB the system might manifest itself as a symbiotic system with AGB and main-sequence components (Kenyon & Webbink 1984). Owing to the wind mass loss from the system, the separation of the components increases. Both the radius of the primary and the radius of its Roche lobe increase, with the radius of the primary growing faster until the primary overflows its Roche lobe (RLOF) close to the tip of the AGB. Both because the primary at this time has a deep convective envelope and the mass ratio of the components is high, the dynamical mass loss is unavoidable (Hjellming & Webbink 1987) and the shedding of the envelope results in formation of a common envelope (CE) and a reduction of the separation of the components due to angular momentum loss in CE. What remains of the primary after this episode is the more massive component of the core of TS 01. The system remains wide enough so that other component may evolve to become a giant star too and experience RLOF close to the tip of the AGB, forming the current *cool* component. The matter ejected during the second CE episode is now observed as a planetary nebula.

We now present numerical estimates that argue in favor of the feasibility of a scenario such as that just described. In our evolutionary simulations, we use the "rapid evolutionary code" SSE (Hurley et al. 2000) based on the analytical fits to detailed grids of full stellar models. We use the SSE code because detailed evolutionary tracks for low-metallicity stars with $M < 1\,\mathrm{M}_\odot$ have yet to be computed. Comparison with data for more massive stars (e. g. Weiss & Ferguson 2009) shows that the initial-final mass relations used by us agree with the results of sophisticated, full evolutionary computations to within $\simeq 10$ per cent and, hence, qualitatively, the resulting scenario must be robust. We note also, that the results of evolutionary calculations depend heavily on the opacities used for the models.

Stasińska et al. (2009) estimate that the metallicity of TS 01 ranges from 1/12 to 1/30 of the solar value (taken as $Z_\odot$=0.014; Lodders et al. 2009). For our calculations we accepted Z=0.001 as a proxy to the metallicity of TS 01, since our goal is to demonstrate the possibility of forming a system similar to TS 01, rather than attempt to reproduce precise values for parameters that are still quite uncertain.

The second CE episode, which produced the current *cool* component, followed RLOF by its precursor close to the tip of AGB. Using SSE, we find that, for Z=0.001, stars with a ZAMS mass exceeding $0.89\,\mathrm{M}_\odot$ evolve to the tip of AGB in less than 10 Gyr. At the tip of the AGB, a star with $M_{\mathrm{ZAMS}} = 0.89\,\mathrm{M}_\odot$ has a mass of 0.60 $\mathrm{M}_\odot$ and a core mass of 0.54 $\mathrm{M}_\odot$, which is coincidentally similar to the estimated mass of the *cool* compo-

[8] Below, we use the terms "primary" and "secondary" for components that were, respectively, more and less massive at ZAMS. As we will show further, "primary" is precursor of the *hot* component, while "secondary" is precursor of the *cool* component.

[9] The first giant branch, in which the helium nucleus is formed but not burning yet.

Table 4: Summary of parameters of TS 01.

Method	T_{cool} $\times 10e3$ K	M_{cool} $M_\odot$	R_{cool} $R_\odot$	$\log g_{cool}$	T_{hot} $\times 10e3$ K	M_{hot} $M_\odot$	R_{hot} $R_\odot$	used data
FITSB2	60 ± 5			5.17 ± 0.07				GEMINI, CFHT
SED 2BB fit	55 ± 7		0.43*		152–175		0.04–0.12	SDSS, HST, FUSE, XMM
Evolution		0.53 ± 0.01						Weiss & Ferguson (2009)
NIGHTFALL	57 *	0.54 *	0.43 ± 0.02	5.03 ± 0.02	160–200	0.71–0.93	0.1–0.13	Calar-Alto, GEMINI, CFHT
TMAP	55 ± 5			4.9 ± 0.5				GEMINI, HST

*Fixed parameters in corresponding fits

nent in TS 01. Motivated by Fig. 13, we adopt a total system mass of $1.39\,M_\odot$. Given a mass of $0.54\,M_\odot$ for the the *cool* component, the mass of *hot* component is then $\approx 0.85\,M_\odot$, corresponding to an initial mass of $2.5\,M_\odot$.

At the tip of AGB, the precursor of the *cool* component had a radius $R \approx 140\,R_\odot$. Using the formula from Eggleton (1983) for the dimensionless radius of the Roche lobe r_L, we estimate that the pre-CE separation of components was about 400 $R_\odot$. The variation of the separation of components in CEs may be described by the formula suggested by Webbink (1984):

$$\frac{a_f}{a_0} = \frac{M_c}{M_2}\left[1 + \frac{2}{\alpha_{ce}\lambda r_{2,L}}\frac{M_2 - M_c}{M_1}\right]^{-1}, \qquad (1)$$

where M_2 and M_c are initial and final masses of mass-losing component (the donor), M_1 is the mass of companion, $\alpha_{ce}\lambda$ is the product of efficiency of common envelope expulsion α_{ce} and the structural parameter λ which characterizes binding energy of the donor envelope. $r_{2,L}$ is the fractional Roche lobe radius of the donor. The reduction of the separation from $a_0 \approx 400$ $R_\odot$ to the current $a_f \approx 1.3$ $R_\odot$ is possible if $\alpha_{ce}\lambda \approx 0.0015$, i.e., is extremely low.

In the stage preceding the common envelope, the system contained an AGB star and a massive (*hot*) companion accreting from the wind. In this stage, the system could be identified with a symbiotic star (Tutukov & Yungelson 1976; Kenyon & Webbink 1984; Yungelson et al. 1995; Lü et al. 2006). Accretion reheated white dwarf and resulted initially in unstable and later in stable hydrogen burning at the surface of white dwarf. Energy release by nuclear burning also contributed to the heating of white dwarf.

It is plausible that currently *hot* component still burns remainders of hydrogen accreted in this stage. During the symbiotic stage, the precursor of the *cool* component lost about $0.29\,M_\odot$ via a wind. Accretion from the wind in symbiotic systems is inefficient ($\sim 10\%$ de Val-Borro et al. 2009) and we may safely assume that all mass lost by the donor was lost from the system taking away specific angular momentum of the donor ("Jeans mode of mass ejection") and that the mass of the *hot* component did not change. Jeans mode of mass ejection has an invariant $a \times (M_1 + M_2)$ and, hence, the separation of the components in the beginning of the symbiotic stage was $320\,R_\odot$. This separation, $320\,R_\odot$, is also the separation of components after the first CE stage, which aborted the ascend of AGB by the initially more massive component close to the tip of the AGB. Before the first CE stage, the mass of the star decreased via wind mass-loss from $2.5\,M_\odot$ to $1.29\,M_\odot$. Its radius at the tip of the AGB was 495 $R_\odot$. Like for the second RLOF episode, from the condition of RLOF we may estimate that the separation of the components at the beginning of the first RLOF was $1200\,R_\odot$. The reduction of the separation in the first CE phase from $1200\,R_\odot$ to $320\,R_\odot$ implies $\alpha_{ce}\lambda \simeq 1.5$. The first CE episode could also have been preceded by a symbiotic stage. We again assume that all mass lost by the donor was lost from the system via the Jeans mode of mass ejection. We then estimate the initial separation of components as close to $770\,R_\odot$. We neglect the wind mass loss during the first red giant stage, which is only several $0.01\,M_\odot$ for $M_0 \simeq 2.5\,M_\odot$. The numerical data is summarized in the upper part of Table 5 (scenario I) and is presented in a form of a cartoon in Fig. 15.

An apparent problem with the suggested scenario is the large difference in $\alpha_{ce}\lambda$ for the common envelope stages. While $\alpha_{ce}\lambda \sim 1$ is typical for WD+MS stars with periods below about 10 days,

Table 5: Numerical evolutionary scenarios for TS 01. The upper part of the Table shows scenario (I) based on energy balance formalism of Webbink (1984), while lower part of the Table presents scenario (II) based on angular momentum balance formalism of Nelemans et al. (2000)

M_1 $M_\odot$	M_2 $M_\odot$	a $R_\odot$	Comment
2.5	0.89	770	ZAMS
1.29	0.89	1200	The end of AGB ascend by the primary, beginning of the first RLOF (CE)
0.86	0.89	320	The end of the first CE, $\alpha_{ce} \approx 1.5$, formation of the first WD, beginning of the symbiotic stage
0.86	0.60	400	The end of the symbiotic stage; RLOF (CE); ejection of PN, $\alpha_{ce}\lambda \sim 0.001$
0.86	0.54	1.3	Present state
5.0	0.89	150	ZAMS
5.0	0.89	150	The end of FGB ascend by the primary, beginning of the first RLOF (CE)
0.87	0.89	240	The end of the first CE, $\gamma \approx 1.2$, formation of He-star evolving into first WD, beginning of the symbiotic stage
0.87	0.73	260	The end of secondary evolution in E-AGB; RLOF (CE); ejection of PN, $\alpha_{ce}\lambda \sim 0.01$
0.87	0.53	1.3	Present state

which are supposed to form via one common envelope stage and implies that the energy spent on the expulsion of the common envelope is comparable to the orbital energy of the initial binary (Nelemans & Tout 2005), $\alpha_{ce}\lambda \sim 0.001$ during the second CE episode appears atypically low. However, common envelopes remain virtually *terra incognita* in stellar evolution and we cannot exclude a significant difference in the interaction of the AGB star envelope with a MS or a WD companion, which differ in structure and, most importantly, by two orders of magnitude in radius (whereas the drag force is $\propto R^2$).

An alternative scenario for TS 01 assumes that present *cool* component had a precursor with ZAMS mass of $0.89\,M_\odot$, while the *hot* component descended from a helium star which was formed by RLOF close to the tip of FGB. For instance, a $5\,M_\odot$ star has a maximum He-core mass of $0.87\,M_\odot$ which, presumably, evolves into a CO WD of the same mass[10]. Thus, the initial system could contain a $5\,M_\odot$ component and a $0.89\,M_\odot$ component and after the 1st CE to become a $(0.87{+}0.89)\,M_\odot$ system. If $5\,M_\odot$ star filled Roche lobe close to the tip of FGB when it radius was close to $80\,R_\odot$, prior to RLOF separation of components have had to be close to $150\,R_\odot$.

If the precursor of the *cool* component was an AGB star, the smallest radius with which it could overfill its Roche lobe at E-AGB was $\approx 100\,R_\odot$. At this moment the total mass of the star was $0.73\,M_\odot$, the mass of the core – $0.53\,M_\odot$, and from the RLOF condition we obtain that the separation of the stars was $\approx 260\,R_\odot$. In the second CE the separation decreased from $260\,R_\odot$ to $1.5\,R_\odot$ by ejection of $0.2\,M_\odot$. This is possible if $\alpha_{ce}\lambda \approx 0.01$, i.e. an order of magnitude larger than in the first scenario.

If we account for Jeans-mode mass loss by the precursor of the *cool* component we obtain that, after the first CE, the separation of components was close to $240\,R_\odot$. Thus we arrive to an apparent controversy: in the suggested scenario, in the

[10]We set the mass of WD equal to the mass of its He-star precursor, thus implicitly neglecting the possibility of re-expansion of the He-star after exhaustion of helium in its core. Such an expansion with formation of a shallow CE and almost negligible mass loss was discovered by Iben & Tutukov (1985) for solar metallicity stars, but its possibility was never explored for non-solar metallicities.

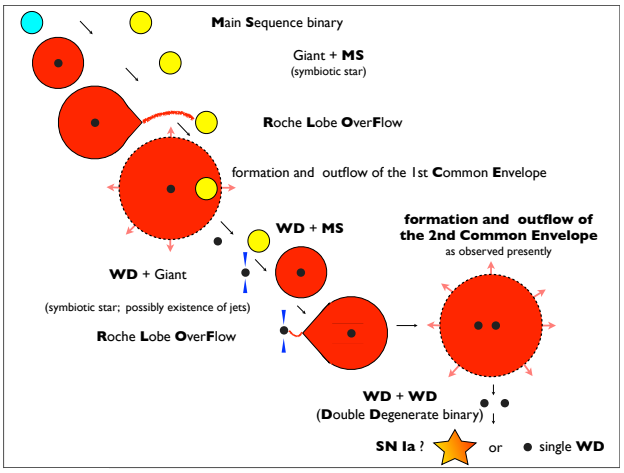

Fig. 15.— Cartoon depicting the evolution of TS 01.

first CE episode, the separation of the components had to *increase* from 150 to 240 $R_\odot$!

However, it was noticed by Nelemans et al. (2000) and later confirmed by Nelemans & Tout (2005) that using Eq. (1) for the description of the outcome of unstable mass exchange between a giant and a MS-star often does not allow to reproduce well measured parameters of many post-CE binaries. As an alternative, Nelemans et al. (2000) suggested to estimate the post-CE separations of components using an equation for angular momentum balance:

$$J_\mathrm{i} - J_\mathrm{f} = \gamma J_\mathrm{i} \frac{\Delta M}{M_\mathrm{tot}}. \qquad (2)$$

Here J is the orbital angular momentum, subscripts i and f denote the initial and final values of the momentum, ΔM is the mass lost from the system (the envelope of the donor), and M_tot is total initial mass of the system. Thus, a single parameter γ describes the fraction of initial specific orbital angular momentum of the binary taken away by outflowing matter. This "γ-formalism" leads to:

$$\frac{a_\mathrm{f}}{a_0} = \left(\frac{M_1}{M_\mathrm{c}}\right)^2 \left(\frac{M_\mathrm{c}+M_2}{M_\mathrm{tot}}\right) \left(1-\gamma\frac{\Delta M}{M_\mathrm{tot}}\right)^2. \qquad (3)$$

Here M_c is the mass of the core of the mass-losing component. An increase of the separation during the CE from 150 $R_\odot$ to 240 $R_\odot$ is possible if $\gamma \approx 1.2$. Rather similar combinations of γ for the first CE and $\alpha_{ce}\lambda$ for the second one were found for some systems studied by Nelemans & Tout (2005, see their Figs. 1 and 5).

4.2. Common Envelope Remnant vs. Single Star Evolution through post- AGB phase.

Ejection of a common envelope definitely differs from formation of a planetary nebula by the usually assumed superwind mechanism. In that context, it is interesting to compare parameters of the *cool* star deduced here with the evolutionary models for post-AGB stars. Given that the *cool* component of TS01 nearly fills its Roche lobe and that it is currently contracting, it has only recently terminated the phase of common envelope evolution. The structure and mass of its envelope might be very different from that of a single star passing through the early epochs of planetary nebula nucleus stage. Here we compare the derived parameters of the *cool* component of TS 01 with two sets of models of remnants of single stars with initial masses of 1.0 $M_\odot$(lower progenitor masses are not available in the literature). Based on estimated abundances, we selected the models $M = 0.623\,M_\odot$, Z=0.001 Vassiliadis & Wood (1994) and $M = 0.547\,M_\odot$, Z=0.0005 Weiss & Ferguson (2009). These models agree well regarding the time-dependence of heating of the core of a post-AGB star (lower right panel of Fig. 16). TS 01 has T_eff similar to them at the age of ≈ 6000 yr. This age estimate is in a good agreement with the age deduced from the expansion velocity and distance to the planetary nebula (Stasińska et al. 2009).

Compared to the most modern and the closest in mass model of Weiss & Ferguson (2009), the nucleus of TS 01 is slightly more compact (by 0.05 dex) and significantly (by more than 0.3 dex) less luminous. Since the main source of luminosity of post-AGB stars is hydrogen burning, this may mean that common envelope remnants may have less massive H/He envelopes around degenerate cores than their post-AGB counterparts.

This comparison clearly indicates that evolution in common envelopes might alter evolution of stars in close binary systems compared to single stars and a more complete analysis of TS01 is warranted than can be made with single star models.

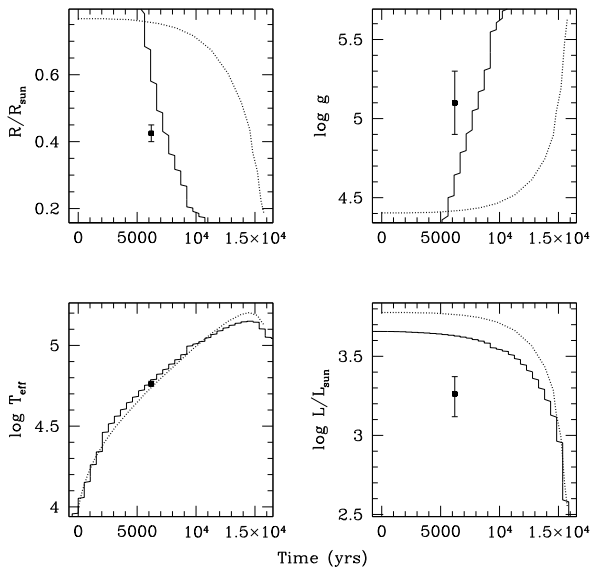

Fig. 16.— Various parameters of the models of post-AGB stars vs. time. Solid line is for the $M = 0.547\,M_\odot$, Z=0.0005 model Weiss & Ferguson (2009), dotted line is for the $M = 0.623\,M_\odot$, Z=0.001model Vassiliadis & Wood (1994). TS 01 is marked by squares with error bars at age of (~ 6000 yr), appropriate to its effective temperature.

4.3. TS 01 and SNe Ia

The evolutionary path suggested for TS 01 includes a stage of a symbiotic star which is considered as one of the routes to SN Ia (e. g. Tutukov & Yungelson 1976; Iben & Tutukov 1984; Munari & Renzini 1992). However, conditions in symbiotic systems are not favorable for an efficient accumulation of matter by the white dwarf components. Accretion from the wind typically allows only several per cent of the mass lost by the donor to be accreted. In the numerical scenario above, the maximum mass-loss rate by the progenitor of the *cool* component estimated by means of SSE is close to 2×10^{-7} $M_\odot$ yr^{-1}. This means that for about 10 Gyr the white-dwarf (*hot*) component stays in the regime of unstable thermonuclear burning (of Novae eruptions) (Nomoto 1982) and instead of accumulating mass it may erode. Conditions for accretion "improve" if the accretor is located in the zone of acceleration of the stellar wind, which requires the proximity of the donor surface to the Roche lobe (Yungelson et al. 1995), or if the stellar wind is pumped close to the Roche lobe by pulsations and still remains slow (Podsiadlowski & Mohamed 2007). Then accretion efficiency may become close to 100%. Using Bondi & Hoyle (1944) formalism for wind accretion, accounting for possible location of accretor in the wind acceleration zone and taking accretion rate limits for stable hydrogen burning after Nomoto (1982), we estimate that the system could accrete steady for the last several 100 000 yr prior to CE and accumulate only several $0.01\,M_\odot$. In a more general context, the circumstances listed above prevent symbiotic stars from being efficient progenitors of SN Ia and the estimated rate of occurrence of SN Ia in these systems is only $\sim 10^{-6}\,\mathrm{yr}^{-1}$ on a Galactic scale (e. g. Yungelson 2005).

For a fraction of time between Novae eruptions and in steady-burning regime the system can manifest itself as a supersoft X-ray source (e. g van den Heuvel et al. 1992; Truran & Glasner 1995; Yungelson et al. 1996).

Note that, during the stage of accretion onto the current *hot* component, the matter could inflow onto the equatorial regions of the dwarf while it outflows from the polar regions. The "bars" seen in TS 01's nebular shell (Stasińska et al. 2009) may be the remnants of jets that once existed in the system.

Figure 17 shows the positions of double-degenerate systems with known parameters in the $M_{\rm tot} - P_{\rm orb}$ plane. As well, positions of several sdB stars with white dwarf companions are shown. The latter systems will turn into double-degenerates after completion of helium burning in sdB stars. Thus, its short orbital period of 3.92 hr and its total mass close to the Chandrasekhar mass makes TS 01 very promising candidate progenitor for a SN Ia in the double-degenerate scenario for these events (Tutukov & Yungelson 1981; Iben & Tutukov 1984; Webbink 1984). For instance, the merger of components will occur in ≈660 Myr in the first evolutionary scenario suggested above and in ≈1.2 Gyr in the second scenario. The only "competitor" to TS 01 is sdB+WD system KPD 1930+2752 with orbital period 2.28 hr, $M_{\rm sdB} = 0.45$ – $0.52\,M_\odot$, $M_{\rm tot} = 1.36$ – $1.48\,M_\odot$ (Geier et al. 2007). In the latter system, subdwarf star will turn into a WD in

≈(220 – 140) Myr, see Yungelson (2008) for estimates of lifetime of sdB stars. It will take two WD several tens of Myr more to merge. Favourable conditions for central carbon ignition may come to fruition just in systems with low mass ratios of components (Yoon et al. 2007), like TS 01 and KPD 1930+2752.

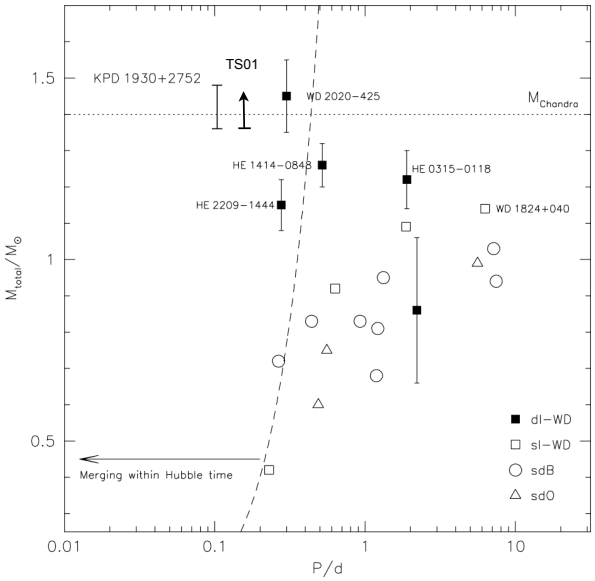

Fig. 17.— Positions of the known detached double-degenerate systems (DD) and subdwarf+white dwarf systems which will turn into double degenerates. d1 – DD with two visible spectra, s1 – DD with one visible spectrum. Updated figure from Geier et al. (2007). The position of TS 01 is marked by an arrow, indicating the tendency of better fit to the observed data with increase of total mass of the binary. The minimum value $M_{\rm tot} \geq 1.35 M_\odot$ corresponds to the leveling of χ^2 slope in Fig. 13. We consider the values at plateau in the $\chi^2 - M_{\rm tot}$ dependance as a range of best solutions.

.

5. Conclusions.

After a decade of intense study, we have achieved a good understanding of an object whose discovery spectrum was misidentified and incomprehensible in 1997. Since then, the object has been observed at practically all wavelengths with the help of the most advanced instruments. This paper accompanies Stasińska et al. (2009), which focuses upon the chemical composition and ionization state of TS 01's nebular shell. Here, we focus on the nature of the close binary nucleus of the PN.

TS 01 is one of the shortest period systems among the double-degenerate or pre-double-degenerate systems, with an orbital period of 3.924 hours This fact would not have caused confusion if the older of the components were significantly cooler than the core of the star that most recently ejected its envelope to form the current PN. However, observations and analysis clearly demonstrate that TS 01's nucleus is comprised of two compact stars, both extremely hot and thus, both being sources of ionization for the nebula. This unusual phenomenon created confusion and misinterpretation of the object in the past. Nevertheless, the correct understanding of the ionization source does not change the essence of those previous interpretations. TS 01 remains a PN with a record low oxygen abundance (Stasińska et al. 2009).

According to our scenario, TS 01 evolved through two common envelope episodes. In the current stage we are observing the remainders of the second common envelope as a PN. The core of the envelope-shedding post-AGB star is in the process of contraction and heating up. At the present time, it nearly fills its Roche lobe and has an ellipsoidal shape. Before the last CE episode, the more massive component, which became a white dwarf earlier, underwent a period during which it accreted mass at a high rate and burned hydrogen steady. Since then it stays close to the temperatures range typical for supersoft X-ray sources. Its properties make TS 01 one of the softest X-ray sources ever, similar to Lin 358 (Orio et al. 2007).

The parameters of the binary system were deduced using a wealth of information and via three independent routes. Although, each of these methods requires its own assumptions and each alone produces ambiguous results, in combination, they converge to values with unusual precision. Using the spectral energy distribution, from the far infrared to X-rays, the light and radial velocity curves, and by fitting atmospheric models to the stellar absorption features of the *cool* component, we find that the *cool* component has a mass of

$0.54 \pm 0.2\,M_\odot$, an average $T_{\rm eff}$ of $58\,000 \pm 3\,000$ K, a mean radius of $0.43 \pm 0.3\,R_\odot$, and $\log g = 5.0 \pm 0.3$. The *cool* component nearly fills its Roche lobe. The temperature and gravity over the surface of the *cool* component are not homogeneous.

The chemical composition of the *cool* component from atmosphere model fitting was determined as: 12 + log He/H = 10.95 and 12 + log C/H = 7.20, with an uncertainty of about 0.3 dex, and upper limits 12 + log N/H < 6.92 and 12 + log O/H < 6.80. Overall, the agreement with the abundances found in the nebula by Stasińska et al. (2009) is very good, except for the carbon abundance, which is found to be higher in the nebula for a reason yet not understood.

The parameters for the *hot* component are less certain. It is fairly clear that the spectral energy distributions of real stars at such high temperatures depart from that of a black body. The range of temperatures that we determined for the *hot* component spans 160–200 kK. It seems that the real object acts like a 180-200 kK blackbody in the X-ray range but appears as a 160 kK blackbody in the UV/optical range. Uncertainty in its temperature leads to uncertainty in its size, but it is obvious from our calculations that the *hot* component is larger than normal for a white dwarf, $R_{hot} > 0.1\,R_\odot$, and is probably bloated as a result of intense accretion in the recent past. However, we have indirect information on the hot component through photoionization modeling by reproducing the intensities of the lines emitted by the nebula (Stasińska et al. 2009). We estimate the distance to the object as ~ 21 kpc, and our most reasonable luminosity estimate for the X-ray component is $\sim 10^4\,L_\odot$, appropriate for a supersoft X-ray source.

The total mass of the binary is very close to Chandrasekhar limit. This makes TS 01 one of the best of the known candidates for the progenitor of a type Ia supernova.

We appreciate assistance of J.Greiner helping to check the ROSAT data. R.Wichmann kindly clarified our inquires about *Nightfall*. GT acknowledges UC-MEXUS grant allowing his visit to UCSD and hospitality of Center of Astrophysics and Space Science during the visit. JT and GT were supported by a grant NNX07AQ12G associated with the XMM-*Newton* observations. GT acknowledges CONACyT financial support from project 45847 and PAPIIT 101506 . LRY is supported by RFBR grant 07-02-00454 and Presidium of the Russian Academy of Sciences Program "Origin, Evolution and Structure of the Universe Objects". VS thanks DFG for financial support (grant SFB/Transregio 7 "Gravitational Wave Astronomy"), and for partial support President's programme for support of leading science schools (grant NSh-4224.2008.2), and RBRF(grant 09-02-97013-p-povolzh'e-a). T.R. was supported by the German Astrophysical Virtual Observatory (GAVO) project of the German Federal Ministry of Education and Research (BMBF) under grant 05 AC6VTB and by the German Aerospace Center (DLR) under grant 05 OR 0806. MGR gratefully acknowledges financial support throughout this project from CONACyT grants 43121, 49447, and 82066 and DGAPA-UNAM grants 108406, 108506, 112103, and 116908.

Facilities: XMM, HST (STIS), Gemini, CFHT, SDSS, Calar-Alto(BUSCA), OAN SPM.

REFERENCES

Arnaud, K. A. 1996, in Astronomical Society of the Pacific Conference Series, Vol. 101, Astronomical Data Analysis Software and Systems V, ed. G. H. Jacoby & J. Barnes, 17–+

Bloecker, T. 1995, A&A, 299, 755

Bondi, H., & Hoyle, F. 1944, MNRAS, 104, 273

De Marco, O., Hillwig, T. C., & Smith, A. J. 2008, AJ, 136, 323

de Val-Borro, M., Karovska, M., & Sasselov, D. 2009, ApJ, 700, 1148

Dickey, J. M., & Lockman, F. J. 1990, ARA&A, 28, 215

Djurasevic, G. 1992, Ap&SS, 196, 241

Eggleton, P. P. 1983, ApJ, 268, 368

Geier, S., Nesslinger, S., Heber, U., Przybilla, N., Napiwotzki, R., & Kudritzki, R.-P. 2007, A&A, 464, 299

Heise, J., van Teeseling, A., & Kahabka, P. 1994, A&A, 288, L45

Hjellming, M. S., & Webbink, R. F. 1987, ApJ, 318, 794

Howarth, I. D., & Wilson, B. 1983, MNRAS, 202, 347

Hurley, J. R., Pols, O. R., & Tout, C. A. 2000, MNRAS, 315, 543

Iben, I., & Tutukov, A. V. 1984, ApJS, 54, 335

—. 1985, ApJS, 58, 661

Iben, Jr., I. 1982, ApJ, 259, 244

Ibragimov, A. A., Suleimanov, V. F., Vikhlinin, A., & Sakhibullin, N. A. 2003, Astronomy Reports, 47, 186

Jacoby, G. H., Feldmeier, J. J., Claver, C. F., Garnavich, P. M., Noriega-Crespo, A., Bond, H. E., & Quinn, J. 2002, AJ, 124, 3340

Kalberla, P. M. W., Burton, W. B., Hartmann, D., Arnal, E. M., Bajaja, E., Morras, R., & Pöppel, W. G. L. 2005, A&A, 440, 775

Kenyon, S. J., & Webbink, R. F. 1984, ApJ, 279, 252

Lodders, K., Palme, H., & Gail, H. . 2009, ArXiv e-prints

Lü, G., Yungelson, L., & Han, Z. 2006, MNRAS, 372, 1389

Marín-Franch, A., Aparicio, A., Piotto, G., Rosenberg, A., Chaboyer, B., Sarajedini, A., Siegel, M., Anderson, J., Bedin, L. R., Dotter, A., Hempel, M., King, I., Majewski, S., Milone, A. P., Paust, N., & Reid, I. N. 2009, ApJ, 694, 1498

Mateos, S., Saxton, R. D., Read, A. M., & Sembay, S. 2009, A&A, 496, 879

Munari, U., & Renzini, A. 1992, ApJ, 397, L87

Napiwotzki, R., Tovmassian, G., Richer, M. G., Stasińska, G., Peña, M., Drechsel, H., Dreizler, S., & Rauch, T. 2005, in American Institute of Physics Conference Series, Vol. 804, Planetary Nebulae as Astronomical Tools, ed. R. Szczerba, G. Stasińska, & S. K. Gorny, 173–176

Napiwotzki, R., Yungelson, L., Nelemans, G., Marsh, T. R., Leibundgut, B., Renzini, R., Homeier, D., Koester, D., Moehler, S., Christlieb, N., Reimers, D., Drechsel, H., Heber, U., Karl, C., & Pauli, E.-M. 2004, in Astronomical Society of the Pacific Conference Series, Vol. 318, Spectroscopically and Spatially Resolving the Components of the Close Binary Stars, ed. R. W. Hilditch, H. Hensberge, & K. Pavlovski, 402–410

Nelemans, G., & Tout, C. A. 2005, MNRAS, 356, 753

Nelemans, G., Verbunt, F., Yungelson, L. R., & Portegies Zwart, S. F. 2000, A&A, 360, 1011

Nomoto, K. 1982, ApJ, 253, 798

Orio, M., Zezas, A., Munari, U., Siviero, A., & Tepedelenlioglu, E. 2007, ApJ, 661, 1105

Péquignot, D., & Tsamis, Y. G. 2005, A&A, 430, 187

Podsiadlowski, P., & Mohamed, S. 2007, Baltic Astronomy, 16, 26

Rauch, T. 2008, A&A, 481, 807

Rauch, T., & Deetjen, J. L. 2003, in Astronomical Society of the Pacific Conference Series, Vol. 288, Stellar Atmosphere Modeling, ed. I. Hubeny, D. Mihalas, & K. Werner, 103–+

Richer, M. G., López, J. A., Steffen, W., Tovmassian, G. H., Stasińska, G., & Echevarría, J. 2003, A&A, 410, 911

Richer, M. G., Tovmassian, G., Stasińska, G., Jameson, R. F., Dobbie, P. D., Veillet, C., Gutierrez, C., & Prada, F. 2002, A&A, 395, 929

Schlegel, D. J., Finkbeiner, D. P., & Davis, M. 1998, ApJ, 500, 525

Schoenberner, D. 1983, ApJ, 272, 708

Shimansky, V. V., Borisov, N. V., Sakhibullin, N. A., Suleimanov, V. F., & Stupalov, M. S. 2002, Astronomy Reports, 46, 656

Stasińska, G., Morisset, C., Tovmassian, G., Rauch, T., Richer, M. Peña, M., Szczerba, R., Decressin, T., Charbonnel, C., Yungelson, L., Napiwotzki, R., Simon-Díaz, S., & Jamet, L. 2009, A&A, in press

Stasińska, G., Tovmassian, G. H., Richer, M. G., Peña, M., Napiwotzki, R., Charbonnel, C., & Jamet, L. 2005, in IAU Symposium, Vol. 228, From Lithium to Uranium: Elemental Tracers of Early Cosmic Evolution, ed. V. Hill, P. François, & F. Primas, 323–326

Suleimanov, V. F., & Ibragimov, A. A. 2003, Astronomy Reports, 47, 197

Swartz, D. A., Ghosh, K. K., Suleimanov, V., Tennant, A. F., & Wu, K. 2002, ApJ, 574, 382

Tovmassian, G., Tomsick, J., Napiwotzki, R., Yungelson, L., Stasińska, G., Peña, M., & Richer, M. 2007, ArXiv e-prints

Tovmassian, G., Tomsick, J., Napiwotzki, R., Yungelson, L., Stasińska, G., Peña, M., & Richer, M. 2008, in American Institute of Physics Conference Series, Vol. 968, Astrophysics of Compact Objects, ed. Y.-F. Yuan, X.-D. Li, & D. Lai, 62–65

Tovmassian, G. H., Napiwotzki, R., Richer, M. G., Stasińska, G., Fullerton, A. W., & Rauch, T. 2004, ApJ, 616, 485

Tovmassian, G. H., Stasińska, G., Chavushyan, V. H., Zharikov, S. V., Gutierrez, C., & Prada, F. 2001, A&A, 370, 456

Truran, J. W., & Glasner, S. A. 1995, in Astrophysics and Space Science Library, Vol. 205, Cataclysmic Variables, ed. A. Bianchini, M. della Valle, & M. Orio, 453–+

Tutukov, A., & Yungelson, L. 1981, Nauchn. Informatsii, 49, 3

Tutukov, A. V., & Yungelson, L. R. 1976, Astrophysics, 12, 521

van den Heuvel, E. P. J., Bhattacharya, D., Nomoto, K., & Rappaport, S. A. 1992, A&A, 262, 97

Vassiliadis, E., & Wood, P. R. 1994, ApJS, 92, 125

Webbink, R. F. 1984, ApJ, 277, 355

Weiss, A., & Ferguson, J. W. 2009, A&A, 508, 1343

Werner, K., Deetjen, J. L., Dreizler, S., Nagel, T., Rauch, T., & Schuh, S. L. 2003, in Astronomical Society of the Pacific Conference Series, Vol. 288, Stellar Atmosphere Modeling, ed. I. Hubeny, D. Mihalas, & K. Werner, 31–+

Wilson, R. E., & Devinney, E. J. 1971, ApJ, 166, 605

Yoon, S.-C., Podsiadlowski, P., & Rosswog, S. 2007, MNRAS, 380, 933

Yungelson, L., Livio, M., Truran, J. W., Tutukov, A., & Fedorova, A. 1996, ApJ, 466, 890

Yungelson, L., Livio, M., Tutukov, A., & Kenyon, S. J. 1995, ApJ, 447, 656

Yungelson, L. R. 2005, in Astrophysics and Space Science Library, Vol. 332, White dwarfs: cosmological and galactic probes, ed. E. M. Sion, S. Vennes, & H. L. Shipman, 163–173

Yungelson, L. R. 2008, Astronomy Letters, 34, 620

This 2-column preprint was prepared with the AAS LaTeX macros v5.2.